



Hydrogen production from bioethanol catalyzed by $\text{Ni}_x\text{Mg}_2\text{AlO}_y$ ex-hydrotalcite catalysts

Wenhao Fang^{a,b}, Sébastien Paul^{a,b,c}, Mickaël Capron^{a,b}, Franck Dumeignil^{a,b,d},
Louise Jalowiecki-Duhamel^{a,b,*}

^a Université Lille Nord de France, 59000 Lille, France

^b Centre National de la Recherche Scientifique UMR8181, Unité de Catalyse et Chimie du Solide, UCCS, 59655 Villeneuve d'Ascq, France

^c Ecole Centrale de Lille, 59655 Villeneuve d'Ascq, France

^d Institut Universitaire de France, Maison des Universités, 103 Boulevard Saint-Michel, 75005 Paris, France

ARTICLE INFO

Article history:

Received 23 October 2013

Received in revised form 24 January 2014

Accepted 27 January 2014

Available online 3 February 2014

Keywords:

Hydrogen production

Ethanol

Nickel oxide

Hydrotalcites

Steam reforming

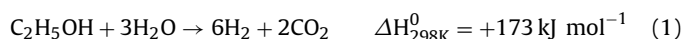
ABSTRACT

H_2 production from ethanol steam reforming ($\text{H}_2\text{O}/\text{EtOH} = 3$) in concentrated conditions (14% of ethanol) was studied over $\text{Ni}_x\text{Mg}_2\text{AlO}_y$ catalysts derived from the hydrotalcite-like precursors. Various physico-chemical techniques were employed to characterize the catalysts, such as XRD, XPS, H_2 -TPR, *in situ* XRD, O_2 -TPO and Raman. Different parameters were carefully analyzed, including reaction temperature, *in situ* activation in H_2 , Ni content and their influence on the efficiency of the catalysts was studied. It is found that well tuning the $\text{Ni}_x\text{Mg}_2\text{AlO}_y$ catalysts and their pre-treatment in H_2 lead to new benefits in both material properties and catalytic performances. The co-precipitation method allows obtaining uniform $\text{Ni}_x\text{Mg}_2\text{AlO}_y$ mixed oxides possessing very active Ni species in small nanoparticles (3–4 nm) of mixed oxides, which are more difficult to reduce compared to bulk NiO due to the strong interactions between Ni cations and Mg and/or Al cations. $\text{Ni}_x\text{Mg}_2\text{AlO}_y$ mixed oxides are shown as active and efficient catalysts for H_2 production from ethanol in the presence of water. In diluted conditions (3% of ethanol) the catalysts enable to totally convert ethanol at 450°C and to provide a CO-free H_2 production of $3.0 \text{ mol mol}_{\text{EtOH}}^{-1}$. A higher and competitive H_2 yield of $5.0 \text{ mol mol}_{\text{EtOH}}^{-1}$ can be achieved at 650°C . The catalysts show good catalytic stability with the time on stream even though solid carbon is formed.

© 2014 Elsevier B.V. All rights reserved.

1. Introduction

The huge potential benefits of H_2 production are recently receiving worldwide interest, because of its high energy-efficiency, pollutants-free emission and diverse applications. However, the hydrogen economy could be clean and sustainable only if it is produced from renewable sources [1–3]. A promising direction for H_2 production is to transform renewable biomass or biomass-derived materials to H_2 -rich gas production [4–6]. Based on a ready fermentation technology, the growing availability, renewability and low cost of bioethanol make it attractive to exploit ethanol as an alternative resource for H_2 production [7–9]. Besides, bioethanol (mainly a mixture of ethanol and water) has featured of high hydrogen content and low toxicity, which lead itself very well to a distributed-production strategy.



* Corresponding author at: Corresponding author. Tel.: +33 0 3 20 33 77 35; fax: +33 0 3 20 33 65 61.

E-mail address: louise.duhamel@univ-lille1.fr (L. Jalowiecki-Duhamel).

The ideal H_2 production from the steam reforming of ethanol (SRE) generates only H_2 and CO_2 [Eq. (1)]. This is a green process because it is considered as a CO_2 neutral process since all CO_2 produced could be recycled back to plants *via* the photosynthesis reaction. Furthermore, instead of producing CO_2 , ethanol can be a carbon source to synthesize carbon nano-materials [10–12], which present outstanding physical and chemical properties and are considered as strategic materials [13]. As a matter of fact, ethanol decomposition (in the absence of water) was studied over different Ni-based catalysts at temperatures between 500 and 800°C to produce hydrogen and carbon nanotubes at the same time [10–12]. In such a context, it could be considered that conjointly to the production of a clean energy, the process not only allows eliminating CO_2 and helping to clean the planet but also producing an added value.

In fact, the SRE process involves quite a complicated reaction network, accompanied by many possible by-products, which mainly depends on the catalyst employed. In such a context, it is highly desirable to develop highly active, selective, stable and low-cost catalysts that are able to efficiently break the C–C and C–H bonds and promote the subsequent formation of H_2 and CO_2 [8,9]. Therefore, it is required to define the important parameters

in order to be able to well tune the catalyst for a given purpose. Moreover, to optimize thermal management of the reformers and build long life and safe reformers that can be used for portable applications like the increasing concern of fuel cells [14], it is necessary to develop catalysts for low-temperature SRE. Till date, many metal catalysts have exhibited active for the SRE reaction, including the noble metals that perform very well at high temperature and the non-noble metals [9,15–17]. Nevertheless, Ni-based catalysts are evidenced to be the most favorable system based on their good capability toward the C–C bond rupture, as well as the low price [18–22]. However, Ni-based catalyst easily suffers deactivation caused by metal sintering and/or carbon deposition with the time on stream. Meanwhile Ni-based catalysts have shown recently promising results in carbon nanotubes production [10–12]. It is well known that the appropriate metal-support interactions are likely to contribute to the activity and the stability of the catalyst. For the conventional oxides-supported Ni catalysts, many efforts have been made to the selection of an optimum support and/or the modification by promoters via the metal-support interactions [23–25].

Recently, an alternative research interest focused on Ni-based catalysts that are derived from the thermal treatment of the hydrotalcite-like compounds [26–29]. As the HT-like compounds can incorporate various metal cations such as Ni^{2+} , Co^{2+} and Cu^{2+} , many researchers have taken them as the catalyst precursor, as the catalyst support [30–33] as well as in direct internal reforming fuel cells [14]. After thermal treatment, the mixed oxides obtained show several unique properties. It allows the materials with large surface area and uniform dispersion of each metal component. It has been reported that the synergetic effect between the metal cations in ex-hydrotalcite catalysts can lead to the resistance to coke formation and the sintering of Ni particles. In this sense, Ni-based ex-hydrotalcite catalysts are able to bring benefit to catalytic process, such as H_2 production from the steam reforming of the biomass-derived compound sources. On the other hand, carbonaceous species can exist in different forms. If the carbon formed during the SRE reaction is kind of carbon nano-materials, it can be regarded as an added value accompanied by H_2 production.

In the past few years, various ternary and quaternary mixed oxide catalysts derived from the HT-like materials have been applied to the SRE reaction, such as Ni–M–Al (M=Mg, Ca, Zn), Ni–Mg–N (N=La, Ce) catalysts [27–29], Co–Mg–Al catalyst [17,34], Cu–Zn–Al catalyst [16], and Cu-, Zn-, La-, Ce-promoted Ni–Mg–Al catalysts [26,35–37]. The common features of these catalytic systems focus on the comparison of the influence of different components and/or promoters on the efficiency of catalysts. A high H_2 production yield between 4.0 and 5.1 $\text{mol mol}_{\text{EtOH}}^{-1}$ has been reported from the above catalytic systems but at temperatures higher than 650 °C with highly diluted feed [26,35,36]. A H_2 yield of 6 $\text{mol mol}_{\text{EtOH}}^{-1}$ is equivalent to 100% in theory [Eq. (1)], but it can never achieve in reality. The highest value for H_2 production that has been reported in the literature is of 5.8 $\text{mol mol}_{\text{EtOH}}^{-1}$, so very close to the theoretical value of 6 $\text{mol mol}_{\text{EtOH}}^{-1}$. It has been obtained at 600 °C over a Ni/CeO₂–ZrO₂ catalyst [38]. Recently Co–Mg–Al hydrotalcite-type catalysts loaded onto ceramic honeycombs have shown very interesting results in the SRE reaction for producing hydrogen under practical conditions with scarce carbon production [34]. However, very few publications report the systematic studies on the most simple and basic ex-hydrotalcite catalysts of Ni–Mg–Al [5,28]. Therefore it is certainly of interest to investigate more deeply the features of the series of $\text{Ni}_x\text{Mg}_2\text{AlO}_y$ catalysts and the application to the SRE reaction.

In the present study, we report the low-priced $\text{Ni}_x\text{Mg}_2\text{AlO}_y$ ex-hydrotalcite catalysts as active and efficient catalyst for H_2 production from SRE. The influences of different parameters are carefully analyzed, such as reaction temperature, *in situ* treatment

in H_2 , and Ni content on the catalyst efficiency. The fresh and spent catalysts, as well as the carbon formation are studied by various physicochemical techniques. It is demonstrated that tuning the catalyst not only allows obtaining the interesting variation in the properties of $\text{Ni}_x\text{Mg}_2\text{AlO}_y$ mixed oxides, but also leads to the promising catalytic activity toward H_2 production. The correlations between the catalyst properties, the catalytic performances and the characterizations are thoroughly discussed.

2. Experimental

2.1. Catalyst preparation

The $\text{Ni}_x\text{Mg}_2\text{AlO}_y$ hydrotalcite-like precursors were prepared by the co-precipitation method by using NaOH/Na₂CO₃ as precipitant. An aqueous mixed solution (1 M) of nitrate metals with a proper molar ratio of Ni:Mg:Al = x:2:1 was added drop-wise into NaOH (1 M) and Na₂CO₃ (0.5 M) mixed solution at room temperature until pH = 8. Then the slurry was kept stirring at 80 °C for 18 h. The solids were recovered by filtration and washing. And then the solids were dried at 120 °C overnight. Finally the $\text{Ni}_x\text{Mg}_2\text{AlO}_y$ mixed oxide catalysts were obtained by the calcination in air at 500 °C for 4 h.

2.2. Catalyst characterization

The metal loadings were analyzed by the ICP-MS technique (Centre d'analyses CNRS Vernaison), and the Ni/Mg/Al molar ratio was then calculated. For $\text{Ni}_x\text{Mg}_2\text{AlO}_y$ mixed oxides, the Ni/ M_T ratio is the nickel molar proportion in all the metals ($M_T = x + 3$, $\text{Ni}/M_T = x/(x + 3)$).

The textural properties were measured by N_2 physisorption at 77 K using a Micromeritics TriStar II 3020 Surface-Area and Porosimetry analyzer. Samples were previously out-gassed under vacuum at 150 °C for 3 h.

XRD analysis was carried out with a Bruker D8 Advance X-ray diffractometer equipped with a fast detector type LynxEye with a copper anticathode. The XRD patterns were registered in the 2 θ domain (10–90°) with a measured step of 0.02°, and the time integration was fixed to 0.3 s. The crystallite size was calculated based on the Scherrer equation.

H_2 -TPR was performed on a Micromeritics Autochem II Chemisorption analyzer, and the hydrogen consumption was measured by a TCD detector. 50 mg of the sample was treated in the 5 vol% H_2 –95 vol% Ar mixture with a flow rate of 30 mL min^{−1}. The temperature was increased to 1000 °C at a heating rate of 10 °C min^{−1}.

XPS analysis was performed on a Thermo VG Escalab 220 XL spectrometer under ultrahigh vacuum, using a twin Al x-ray source (1486.6 eV) at a pass energy of 40 eV. The solids in the form of pellets were fixed on a copper holder with copper tape. The charge effect was adjusted by reference to the C 1s peak at 285 eV and for catalysts after reaction, Al2p was chosen as the reference.

In situ XRD in H_2 was performed on a Bruker D8 Advance type HT1200N X-ray diffractometer equipped with a fast detector type VANTEC with a copper anticathode. A mixture of 3 vol% H_2 –97 vol% Ar is employed with a heating rate of 10 °C min^{−1}.

O_2 -TPO was performed on a Micromeritics Autochem 2920 analyzer. The sample was treated in the 5 vol% O_2 –95 vol% He mixture with a flow rate of 50 mL min^{−1}. The temperature was increased to 1000 °C at a heating rate of 5 °C min^{−1}. The desorption of the species from the sample were traced by an OmniStar GSD 300 O mass spectrometer.

Raman spectra were acquired on a Labram Infinity HORIBA JOBIN YVON Raman spectrometer using a visible laser with an output laser power of $\lambda = 532$ nm at room temperature.

2.3. Catalytic reaction

The catalytic performance was conducted under atmospheric pressure in a fixed-bed up flow reactor. The reactor was a quartz tube (inner diameter 8 mm) with a quartz frit to support the catalyst [18]. Heating of the reactor was provided by a programmable oven. The catalyst (50 mg when not precised) was previously *in situ* treated in pure H₂ for 10 h at a given treatment temperature (T_T). The water–ethanol mixture with a stoichiometric molar ratio of 3 was injected into a heating chamber (vaporizer) by HPLC pump, and then the steam was fed into the reactor by N₂ as carrier with a flow rate of 60 mL min^{−1} (concentrated conditions as default: EtOH/H₂O/N₂ = 14/42/44, or diluted conditions, EtOH/H₂O/N₂ = 3/9/88 when specified). After periods of at least 5 h at each reaction temperature, the temperature was increased consecutively between 200 and 650 °C. The vaporizer and all transfer lines were heated to about 150 °C to prevent condensation in the system. The feed and product outlet gases were analyzed online by gas chromatography (TRACE GC ULTRA) equipped with a thermal-conductivity detector (TCD) and a flame ionization detector (FID).

The influence of *in situ* activation of catalyst was studied by *in situ* pre-treating the catalyst in pure H₂ at different temperatures (250–700 °C) for 10 h, and then the catalyst was tested for SRE.

Catalytic performance was reported after 5 h of reaction based on ethanol conversion (X_{EtOH}), products molar composition (C_i) and hydrogen yield (Y_{H_2}), which were calculated by the following equations [Eqs. (2)–(4)].

$$X_{\text{EtOH}} = \frac{n_{\text{EtOH},\text{in}} - n_{\text{EtOH},\text{out}}}{n_{\text{EtOH},\text{in}}} \times 100\% \quad (2)$$

where $n_{\text{EtOH},\text{in/out}}$ is the molar flow rate of ethanol at the inlet/outlet of the reactor, respectively.

$$C_i = \frac{n_i}{\sum_{\text{products}} n_i} \times 100\% \quad (3)$$

where n_i represents the molar flow rate of product i at the outlet of the reactor.

$$Y_{\text{H}_2} = \frac{n_{\text{H}_2}}{n_{\text{EtOH},\text{in}} X_{\text{EtOH}}} \leq 6 \quad (4)$$

where a yield of 6 mol mol_{EtOH}^{−1} is equivalent to 100% in theory [Eq. (1)].

3. Results and discussion

3.1. Characterizations of Ni_xMg₂AlO_y catalysts

3.1.1. Ni_xMg₂AlO_y catalyst precursors

The XRD patterns of Ni_xMg₂AlO_y catalyst precursors (HT-like compounds) are shown in Fig. 1. Obviously, well-crystallized materials are successfully synthesized by the co-precipitation method. All the precursors exhibit the characteristic diffractions of the layered double hydroxalite or HT-like compounds for (003), (006),

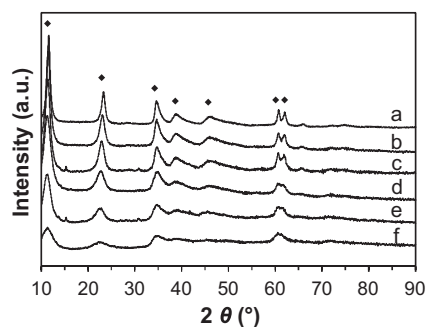


Fig. 1. XRD patterns of Ni_xMg₂AlO_y catalyst precursors. x = a) 0, b) 0.5, c) 1, d) 2, e) 3, f) 4. HT-like phase (◆).

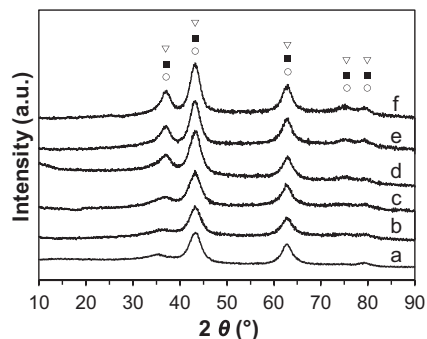


Fig. 2. XRD patterns of Ni_xMg₂AlO_y mixed oxides. x = a) 0, b) 0.5, c) 1, d) 2, e) 3, f) 4. MgO (○), Ni–Mg–O (■), NiO (▽).

(012), (015), (018), (110) and (113) planes, according to 70-2151 JCPDS file. The ternary Ni_xMg₂AlO_y HT-like compounds appear less crystallized than the hydrotalcite (Mg₂AlO_y), which is proved by the shape and broadness of the diffraction peaks depending on the Ni content. The interlayer distance as measured from the position of (003) plane (the first peak), is found to be 0.77 nm for Mg₂AlO_y hydrotalcite. When the Ni content increases, the interlayer distance is found in the range of 0.76–0.77 nm (Table 1). These data are quite similar to the value (0.76 nm for Mg–Al HT) provided by Ogawa and Kaiho [39], and the data (0.77 nm for Ni–Mg–Al HT-like precursor) reported by Li et al. [28]. Ni_xMg₂AlO_y HT-like compounds do not exhibit regular textural parameters related to the Ni content (Table 1). Globally the pore volume and the pore size increase with Ni content, while the specific surface areas are measured from 38 to 76 m² g^{−1}. The highest specific area is obtained on the Ni₁Mg₂AlO_y HT-like compound.

3.1.2. Ni_xMg₂AlO_y mixed oxides

The crystalline phase and structure of Ni_xMg₂AlO_y mixed oxides were investigated by XRD analysis. After calcination at 500 °C, the HT-like structures are destroyed and the precursors are transformed into oxides. As presented in Fig. 2, the diffraction patterns of Ni_xMg₂AlO_y catalysts (x > 0) can be attributed to a mixture of MgO

Table 1
Interlayer distance and textural parameters of Ni_xMg₂AlO_y catalyst precursors.

Precursor ^a	Interlayer distance/nm ^b	S _{BET} /m ² g ^{−1}	Pore volume/cm ³ g ^{−1}	Pore size/nm
Mg ₂ AlO _y	0.77	63	0.15	5.9
Ni _{0.5} Mg ₂ AlO _y	0.77	38	0.08	6.1
Ni ₁ Mg ₂ AlO _y	0.77	76	0.16	6.4
Ni ₂ Mg ₂ AlO _y	0.77	40	0.15	7.8
Ni ₃ Mg ₂ AlO _y	0.76	46	0.23	9.1
Ni ₄ Mg ₂ AlO _y	0.76	56	0.22	14.4

^a Theoretical Ni/Mg/Al molar ratio.

^b Calculated from the (003) plane.

Table 2Surface areas, lattice parameters and particles sizes of $\text{Ni}_x\text{Mg}_2\text{AlO}_y$ mixed oxides.

Catalyst	Ni loading/wt% ^a	Ni/Mg/Al molar ratio ^a	Ni/M _T	$S_{\text{BET}}/\text{m}^2 \text{ g}^{-1}$	Lattice parameter α/nm ^b	Oxide crystal d/nm ^b
Mg_2AlO_y	0	0/2.1/1	0	106	0.42	3.2
$\text{Ni}_{0.5}\text{Mg}_2\text{AlO}_y$	13.2	0.5/2.1/1	0.14	95	0.42	3.4
$\text{Ni}_1\text{Mg}_2\text{AlO}_y$	21.9	1/2.1/1	0.24	127	0.41	3.6
$\text{Ni}_2\text{Mg}_2\text{AlO}_y$	35.7	2/1.7/1	0.43	146	0.39	3.7
$\text{Ni}_3\text{Mg}_2\text{AlO}_y$	43.7	3/2.0/1	0.50	168	0.38	3.9
$\text{Ni}_4\text{Mg}_2\text{AlO}_y$	48.2	4/1.8/1	0.60	180	0.36	4.0

^a Measured by ICP-MS technique.^b Calculated from the (200) plane.

(65-0476 JCPDS file), Ni–Mg–O (24-0712 JCPDS file) and NiO (47-1049 JCPDS file). In fact, the diffraction peaks of MgO, Ni–Mg–O and NiO almost overlap each other, and cannot be well distinguished. None of the relevant peaks corresponding to Al_2O_3 is discovered, which can be due to the high dispersion, amorphous phase of the Al species and/or the insertion of Al into the Ni–Mg–O phase to form the Ni–Mg–Al–O solid solution. A careful examination reveals that the addition of nickel affects not only the intensity of the peaks, but also their broadness. It can be attributed to the incorporation of Ni species into MgO phase via the formation of Ni–Mg–(Al)–O solid solution [27]. As a matter of fact, it has been reported that hydro-talcite, magnesium–aluminum hydroxycarbonate, is a naturally occurring anionic clay that reversibly decomposes upon calcination at high temperature to form a high-surface-area, basic, mixed oxide Mg–Al–O where some of the Mg^{2+} is replaced by Al^{3+} [30–32]. The diffraction patterns become more intense and thinner when the Ni content increases, which is in good agreement with the growing average particles size of the crystal oxide (Table 2). Small nanoparticles are obtained in the series studied with an average particles size varying between 3 and 4 nm. The lattice parameter α obtained for Mg_2AlO_y (0.42 nm) is in agreement with the one reported previously (0.417 nm), as only a slightly smaller value has been obtained compared to the one reported for the bulk MgO (0.421 nm) [32]. The lattice parameter α obtained for the $\text{Ni}_x\text{Mg}_2\text{AlO}_y$ catalysts decrease with increasing the Ni content. A lattice parameter α of 0.41 nm is calculated for the $\text{Ni}_1\text{Mg}_2\text{AlO}_y$ catalyst; while it decreases to 0.36 nm for the $\text{Ni}_4\text{Mg}_2\text{AlO}_y$ catalyst. It may be owing to the substitution of Mg^{2+} cations by Ni^{2+} cations, which leads to the decrease of the average distance of metal ions within the oxides, as a result, the lattice parameter α decreases. As a matter of fact, Ni^{2+} radius (0.069 nm) is smaller than that of Mg^{2+} (0.072 nm).

Table 2 also summarizes Ni/Mg/Al molar ratios and BET surface areas of the catalysts. The Ni/Mg/Al molar ratios are precisely measured by ICP-MS technique and are proved to be nearly exactly the same as the theoretical values in the HT-like precursors, which illustrates that there is no loss of any component during the co-precipitation procedure. The specific surface areas largely expand

after the thermal treatment of HT-like precursors at 500 °C. Larger surface area is measured for the catalyst with higher Ni content, and the $\text{Ni}_4\text{Mg}_2\text{AlO}_y$ catalyst shows the maximum surface area of $180 \text{ m}^2 \text{ g}^{-1}$ in the studied series.

3.1.3. XPS analysis

The Ni2p and O1s core-level spectra of the $\text{Ni}_x\text{Mg}_2\text{AlO}_y$ mixed oxides are presented in Fig. 3, and the binding energies obtained from the XPS spectra are listed in Table 3. The $\text{Ni}_1\text{Mg}_2\text{AlO}_y$ and $\text{Ni}_3\text{Mg}_2\text{AlO}_y$ catalysts as examples exhibit a main emission peak in the Ni2p_{2/3} region. The BE for this peak is found at 855.7 eV for the $\text{Ni}_3\text{Mg}_2\text{AlO}_y$ catalyst, which is very similar to that reported previously for Ni–Mg–Al mixed oxides (855.5 eV) [26]. While the $\text{Ni}_1\text{Mg}_2\text{AlO}_y$ catalyst presents a slightly higher BE at 856.1 eV. This value is higher than the BE reported for bulk NiO (853.7–854.6 eV) in the literature, but very close to that observed for NiAl_2O_4 (856 eV) [40–42]. These results demonstrate the strong interactions between Ni^{2+} species with Al^{3+} species and/or Mg^{2+} species. The XPS results are in good agreement with XRD results that have shown the possible formation of Ni–Mg–(Al)–O solid solution. The electron transfer from nickel to magnesium or aluminum in the structure would thus lead to the shift to a higher BE of 855.7 eV. Besides, the satellite line is visible at 862.1 eV, 6 eV up to the main peak. This 6 eV satellite has been interpreted by a predominant surface plasmon loss due to a two hole $c3d^9 4s^2$ (c is a core hole) final state effect [41]. Therefore, the results clearly show the presence of Ni^{2+} species.

The O1s core level presents one peak with a BE at 531.7 eV for the Mg_2AlO_y and $\text{Ni}_1\text{Mg}_2\text{AlO}_y$ catalysts, whereas two peaks with BE at 530.6 and 531.7 eV are observed for the $\text{Ni}_3\text{Mg}_2\text{AlO}_y$ catalyst (Fig. 3). The peak at 531.7 eV is assigned to the oxygen species in hydroxyl groups while the peak at 530.6 eV corresponds to the typical O^{2-} lattice oxygen species in oxides of NiO and/or MgO and/or Ni–Mg–(Al)–O solid solution [26,40]. The Mg1s line (1303.6 eV) and Al2s line (119.4 eV) present almost no variation with the Ni content, as reported in Table 3. The value of 119.4 eV is higher than the one reported on CeNi–Mg/AlO compounds (118.1 eV) [26], showing

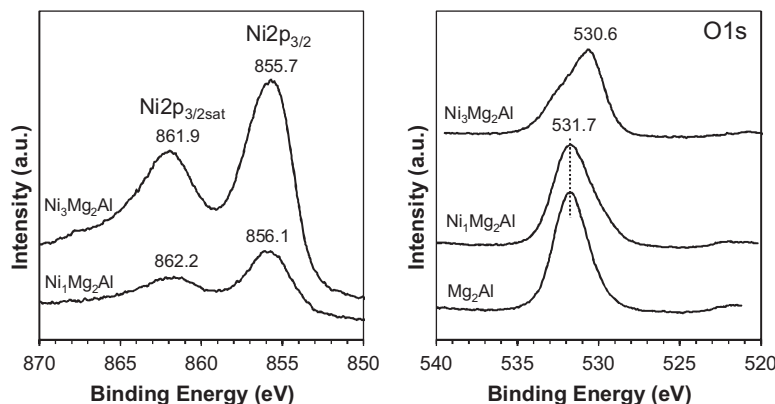
**Fig. 3.** Ni2p and O1s XPS spectra of $\text{Ni}_x\text{Mg}_2\text{AlO}_y$ mixed oxides.

Table 3
XPS parameters of Ni2p, Mg1s, Al2s, and O1s lines.

Catalyst	Ni2p _{3/2} /eV	FWHM (Ni2p _{3/2})/eV	Ni2p _{3/2} satlite/eV	Mg1s/eV	Al2s/eV	O1s/eV	FWHM (O1s)/eV
Mg ₂ AlO _y	—	—	—	1303.6	119.4	531.7	2.48
Ni ₁ Mg ₂ AlO _y	856.1	3.34	862.2	1303.6	119.1	531.7	2.93
Ni ₃ Mg ₂ AlO _y	855.7	3.62	861.9	1303.6	119.4	530.6/531.7	3.08

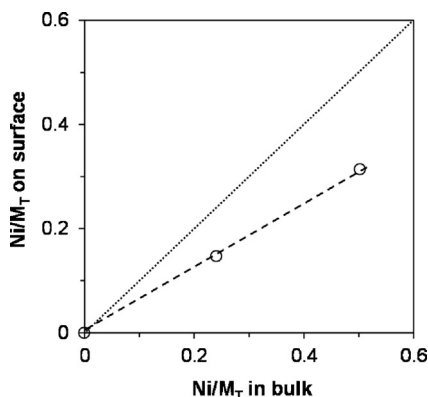


Fig. 4. Variation of the Ni/M_T surface ratio as a function of the Ni/M_T bulk ratio in Ni_xMg₂AlO_y catalysts.

stronger interactions in the present study, which is in agreement with the possible insertion of Al species into the Ni–Mg–O solid solution.

Some quantitative XPS features can provide additional information. Fig. 4 compares the surface Ni molar ratio determined by XPS to the bulk Ni molar ratio measured by ICP, where the variation of Ni concentration with depth in the Ni_xMg₂AlO_y catalysts may be observed. The 45° diagonal line corresponds to the ideal case of a homogeneous distribution of nickel inside the catalysts. It is possible to see that the Ni/M_T ratio on surface is relatively lower than that in bulk, showing a relative surface segregation. On the other hand, the surface Ni/M_T ratio still well respect to the Ni content, presenting a linear relationship. Thus the XPS results are in good agreement with the XRD analysis.

3.1.4. H₂-TPR

The H₂-TPR profiles of Ni_xMg₂AlO_y catalysts are displayed in Fig. 5. A main single broad peak is observed for each sample, no matter what the Ni content is, showing that Ni species are stable and homogeneously distributed in the mixed oxides [14]. The main peak is located in the temperature range of 593–844 °C; moreover the reduction temperature is clearly associated to the Ni content

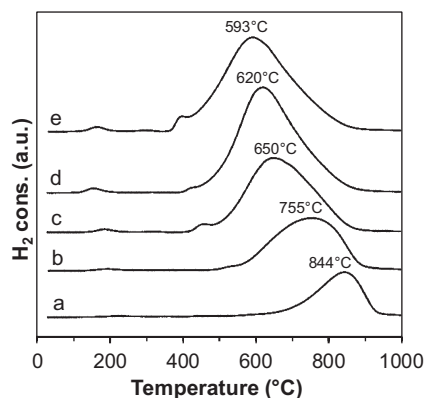


Fig. 5. TPR profiles of Ni_xMg₂AlO_y mixed oxides. x= a) 0.5, b) 1, c) 2, d) 3, e) 4.

of the catalyst. The peaks shift toward lower temperatures with increasing Ni content. The Ni_{0.5}Mg₂AlO_y catalyst presents a reduction peak at 844 °C, whereas for the Ni₄Mg₂AlO_y catalyst the TPR peak appears at a much lower temperature of 593 °C. In other words, the catalyst with higher Ni content is easier to reduce. Besides, it is found that a shoulder peak is emerging in the shape of the curve for higher Ni loadings. A very small TPR peak at about 160 °C is only recorded for the catalysts with Ni/M_T ≥ 0.5.

It is known that bulk NiO basically shows a single broad reduction peak centered at approximately 390 °C, spanning 250–430 °C [28,43]. The existence of NiO phase in Ni_xMg₂AlO_y catalysts is in agreement with XRD analysis, and the proportion of NiO species grows with the higher Ni loadings. It is reasonable to ascribe the small shoulder peak at around 400 °C to the reduction of NiO in Ni_xMg₂AlO_y catalysts, and this peak shifts to lower temperatures by increasing Ni content, probably due to the different chemical environment surrounding Ni species. Compared to bulk NiO, the Ni species in Ni_xMg₂AlO_y mixed oxides are reduced at higher temperatures. For low Ni content the strong interactions between Ni species and other cations either in Ni–Mg–(Al)–O solid solution and/or at the interfaces between small nanoparticles of NiO, MgO and/or Ni–Mg–(Al)–O make the solid more difficult to reduce. However, the Ni content has an effect on the reducibility of the Ni species. When the Ni content increases the Ni_xMg₂AlO_y mixed oxides are more easily reduced (at lower temperature) and the reducibility of the solid becomes closer to that of bulk NiO. However, there are still strong interactions existing between Ni cations and some other cations, because the temperature required for reduction of Ni species is still much higher than the one necessary to reduce bulk NiO, i.e. 593 °C for the Ni₄Mg₂AlO_y catalyst compared to 390 °C for NiO.

In the literature [28,29,36], Ni–Mg–Al ex-hydrotalcite catalysts basically exhibited a single broad reduction peak at high temperatures between 750 and 850 °C, which was interpreted by the strong incorporation of Ni into the Mg–Al support. It has to be noted that to the best of our knowledge, TPR analysis on Ni_xMg₂AlO_y ex-hydrotalcite compound with very high Ni loading has not been reported in the literature. However, it has been already reported that hydrotalcites like compounds with high Ni content require mild reduction temperatures [44]. The components composition has an influence on the reducibility of Ni species. In the current study, the interactions between Ni species and Mg or/and Al species can be significantly modified by tuning the Ni loading; as a consequence, the catalysts with higher Ni loadings are more easily reduced. On a series of Ni/MgO catalysts, it has already been shown that the reducibility increases according to a linear correlation when increasing the metal loading [45], in agreement with the known strong metal-support interaction (SMSI) phenomenon observed at low metal concentration [46]. Further analysis discloses that a linear relationship can be established between the total hydrogen consumption during TPR and the Ni content of Ni_xMg₂AlO_y catalysts (Fig. 6), showing that the quantity of H₂ consumed in TPR analysis is in good agreement with the Ni content of the solids. The H/Ni atomic ratios obtained for the mixed oxides are slightly higher than the theoretical value of 2 necessary to reduce quantitatively NiO into Ni⁰ according to Eq. (5). More specifically, H/Ni atomic ratios between 2.2 and 2.5 are obtained, showing that

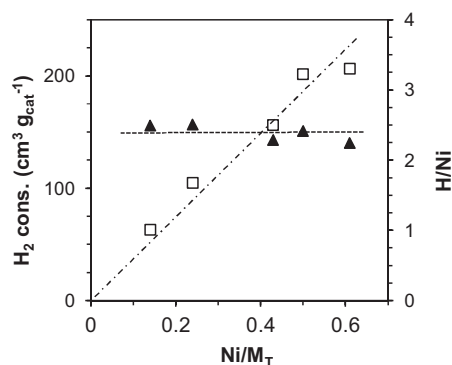
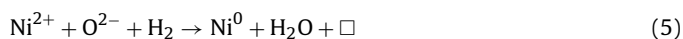


Fig. 6. H_2 consumption (□) and H/Ni atomic ratio (▲) of $\text{Ni}_x\text{Mg}_{2-x}\text{AlO}_y$ mixed oxides during TPR versus Ni content.

some hydrogen species are inserted into the solid that could be explained by a “spill-over effect”.



(with □: anionic vacancy)

3.1.5. *In situ* XRD in H_2

The properties of the $\text{Ni}_x\text{Mg}_{2-x}\text{AlO}_y$ catalysts in presence of H_2 in temperature were also studied by *in situ* XRD in H_2 . Fig. 7 shows the XRD profiles of the $\text{Ni}_3\text{Mg}_2\text{AlO}_y$ and $\text{Ni}_1\text{Mg}_2\text{AlO}_y$ catalysts obtained from the *in situ* treatment in H_2 . Compared to the fresh catalysts, none difference is found in the diffraction patterns obtained at temperatures lower than 450°C in the presence of H_2 . There is a very clear evidence that the metallic Ni^0 phase at $2\theta = 44.5$ and 51.8° (70-1849 JCPDS file) starts to be analyzed on $\text{Ni}_3\text{Mg}_2\text{AlO}_y$ catalyst from the treatment at 450°C for 10 h, which can be respectively attributed to (111) and (200) planes of the metallic nickel. These two diffraction peaks become slightly more intense by further increasing the temperature to 620°C . In addition, a new peak relevant to Ni (220) plane emerges at 76.2° . All the patterns well maintain the diffraction lines of the mixed oxides after treatment in H_2 whatever the temperature, even if they decrease for the $\text{Ni}_3\text{Mg}_2\text{AlO}_y$ catalyst, which implies that the Ni^{2+} species are partially reduced under the analysis conditions examined. In agreement with TPR results no reduction of the $\text{Ni}_1\text{Mg}_2\text{AlO}_y$ catalyst is observed in such conditions by XRD.

Table 4 lists the average sizes of nanoparticles in the $\text{Ni}_3\text{Mg}_2\text{AlO}_y$ catalyst during the *in situ* XRD in H_2 . The Ni^0 average particles size is first measured at about 4.0 nm after treatment in H_2 at 450°C for 10 h. And then, the particles size slightly grows with temperature, finally it reaches about 4.9 nm at 620°C . With regard to oxide crystal nanoparticles, the average particles size

Table 4

Average sizes of nanoparticles in the $\text{Ni}_3\text{Mg}_2\text{AlO}_y$ mixed oxide during *in situ* XRD in H_2 .

Temperature in $\text{H}_2/^\circ\text{C}$	d Oxide crystal/nm ^a	d Ni^0 /nm ^b
Room temperature	3.2	—
163	3.2	—
365	3.7	—
450	3.9	—
450 for 10 h	4.0	4.0
560	4.0	4.5
620	4.0	4.9

^a Calculated from (220) plane.

^b Calculated from Ni^0 (200) plane.

also exhibits a very slight growth depending on the temperature, ranging from 3.2 to 4.0 nm. The values remain relatively close to that of the fresh $\text{Ni}_3\text{Mg}_2\text{AlO}_y$ catalyst showing that the applied preparation allows obtaining nano-compounds constituted of small nanoparticles relatively stable with temperature in reducing treatment. It is necessary to recall that the particles smaller than 2 nm cannot be detected by the XRD technique due to the detection limit. As a good supplement, the *in situ* H_2 -XRD result reaches good agreement with the TPR analysis. It provides phase and structural information to prove that the TPR peak at 620°C is mainly ascribed to the reduction of Ni species. More importantly, it further reveals that treatment in H_2 at 450°C for 10 h of $\text{Ni}_x\text{Mg}_2\text{AlO}_y$ catalysts leads to nanoparticles of NiO and/or mixed oxide (4 nm) accompanied with nanoparticles of metallic nickel Ni^0 (4 nm) only when $x > 1$.

3.2. Catalytic performances

3.2.1. The influence of reaction temperature

The SRE reaction over $\text{Ni}_x\text{Mg}_2\text{AlO}_y$ catalysts was studied in ethanol concentrated conditions ($\text{EtOH}/\text{H}_2\text{O}/\text{N}_2 = 14/42/44$) as a function of reaction temperature, *in situ* activation in H_2 , and Ni content. Fig. 8 reports the catalytic performance of the $\text{Ni}_4\text{Mg}_2\text{AlO}_y$ catalyst as a function of reaction temperature, as an example. 100 mg of catalyst is *in situ* pre-treated in H_2 at 550°C (T_1) and then applied to the SRE reaction. As seen in Fig. 8 a high ethanol conversion at 40% is obtained at a very low temperature of 200°C . Conversion increases with reaction temperature as expected and approaches to 100% at 400°C , exhibiting high activity for SRE. H_2 formation relative to all the gas phase products (dry basis) maintains about 55% (in mol.). It is important to recall that the high conversion of ethanol which is injected in high concentration leads to a high production of gases [21]. This result is ameliorated compared to the recent value reported on $\text{Ni}_{0.5}\text{Mg}_{2.5}\text{Al}$ ex-hydrotalcite catalyst (100 mg) which demonstrated total conversion at 450°C in the presence of 9 mol.% ethanol [37].

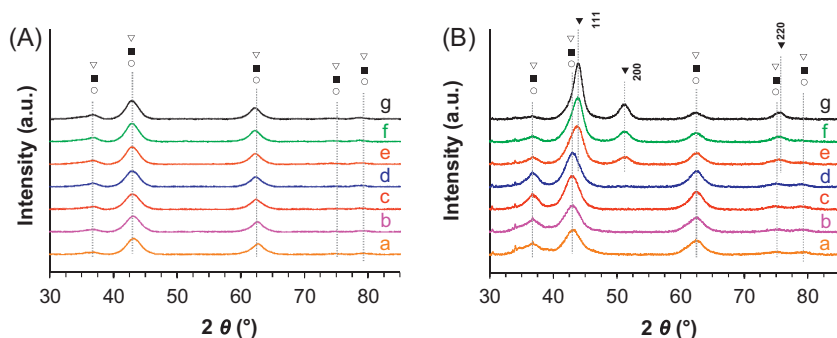


Fig. 7. *In situ* XRD patterns in H_2 for (A) $\text{Ni}_1\text{Mg}_2\text{AlO}_y$ and (B) $\text{Ni}_3\text{Mg}_2\text{AlO}_y$ mixed oxides. a) room temperature, b) 164°C , c) 365°C , d) 450°C , e) 450°C for 10 h, f) 560°C , g) 620°C . MgO (○), Ni-Mg-O (■), NiO (▽), Ni (▼).

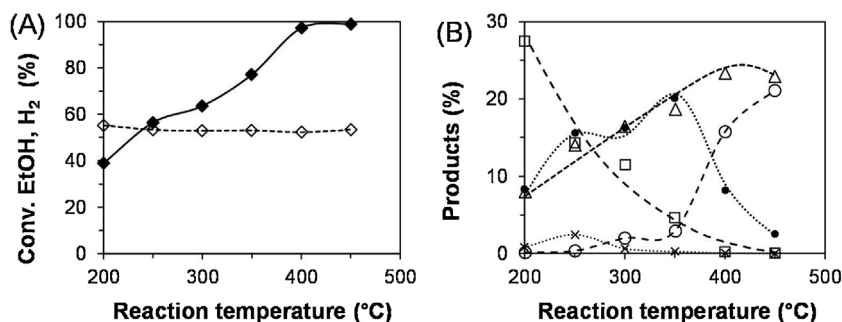


Fig. 8. SRE on the Ni₄Mg₂AlO_y catalyst (100 mg) pre-treated in H₂ at 550 °C versus reaction temperature. Ethanol conversion (◆), H₂ (◇), CO₂ (○), CH₃CHO (□), CO (●), CH₄ (△) and acetone (×) formation.

The other products are acetaldehyde, CO₂, CO and CH₄ (Fig. 8). Acetaldehyde formation shows a significant decline if reaction temperature increases, and finally eliminates at 400 °C. Only trace of CO₂ is examined in the outlet gases at temperature lower than 300 °C. Then CO₂ formation starts to rise from 350 °C and rapidly reaches about 20% at 450 °C. Some other undesirable products, such as CO, CH₄ and acetone, are obtained in the outlet gas. Acetone decreases to zero at 350 °C. CO formation presents a maximum of about 20% at 350 °C; afterwards it declines, which is certainly due to the carbon formation from the disproportionation of CO. CH₄ undergoes a global increase with reaction temperature and reaches a maximum of about 20% at 450 °C.

It seems that the dehydrogenation and decomposition are the main reactions when temperature is lower than 350 °C. It is disclosed that ethanol is more feasible to dehydrogenate to form acetaldehyde and H₂ over the basic catalyst [Eq. (6)]; whereas dehydration to ethylene [Eq. (7)] most likely occurs on acidic sites [9]. Basic oxides, e.g. ex-hydrotalcite compounds favor the acetaldehyde route of ethanol transformation [9]. Over cobalt-based ex-hydrotalcite catalysts, ethanol is first dehydrogenated into a mixture of hydrogen and acetaldehyde [Eq. (6)], and acetaldehyde reacts with steam to yield mainly hydrogen and carbon oxides [Eq. (8)] [34]. In the present study, acetaldehyde could further decompose to CO and CH₄ [Eq. (9)]. In addition, it is possible that ethanol directly decomposes into CO, CH₄ and H₂ over the catalyst possessing strong capability in breaking the C–C bond [Eq. (10)], e.g. Ni-based catalyst [7,18,19]. Acetone can be obtained according to Eq. (11) or by the dehydrogenation of ethanol followed by aldol condensation. When the reaction temperature is higher than 350 °C, SRE starts to be the main reaction. In fact, it is known that high temperature facilitates SRE, while CO transformation by water gas shift [Eq. (12)] is favored at low temperature.

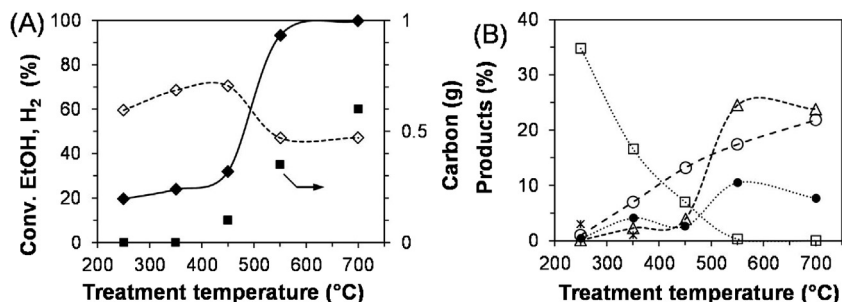
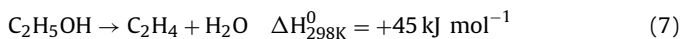
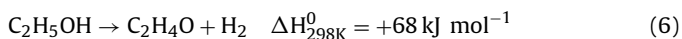
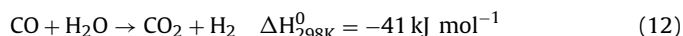
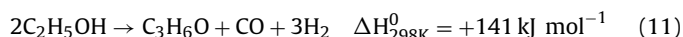
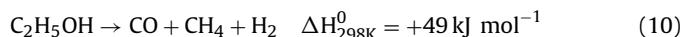
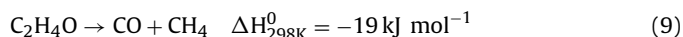


Fig. 9. SRE at 450 °C on the Ni₁Mg₂AlO_y catalyst versus treatment temperature in H₂. Ethanol conversion (◆), H₂ (◇), CO₂ (○), CH₃CHO (□), CO (●), CH₄ (△), C₂H₄ (*) and carbon (■) formation.



The influence of reaction temperature was also studied on Ni_xMg₂AlO_y catalysts with different Ni contents. Globally the same evolution of catalytic behaviors is obtained over the other catalysts with different Ni contents. However, differences in conversion and products distribution due to the influence of Ni content, was studied and discussed later on.

3.2.2. The influence of in situ activation in H₂

The influence of treatment temperature in H₂ was investigated over the Ni₁Mg₂AlO_y catalyst as an example. As illustrated in Fig. 9, ethanol conversion and products distribution show strong dependence on the treatment temperature. Conversion undergoes a slow growth from 20 to 33% when treatment temperature rises from 200 to 450 °C. When treatment temperature further increases to 550 °C, conversion tremendously goes up to 93% and reaches 100% with T_T = 700 °C. H₂ formation first stays relatively stable around 65% and then decreases to about 47% when T_T ≥ 550 °C. Acetaldehyde formation declines while CO₂ formation increases with the treatment temperature. CO and CH₄ formation follow the similar evolution as conversion, that is, there is no big variation when T_T ≤ 450 °C but the maximum values are obtained with T_T = 550 °C. Ethylene formation of about 3% is observed when T_T = 250 °C, which can be derived from the dehydration of ethanol, and it diminishes to less than 1% when T_T = 350 °C. Solid carbon is observed when T_T ≥ 450 °C, and the carbon formation increases almost linearly with the treatment temperature up to 700 °C [Fig. 9 (A)]. As a higher concentration of metallic Ni is expected for high treatment temperature, the result obtained is in agreement with the scarce carbon deposition

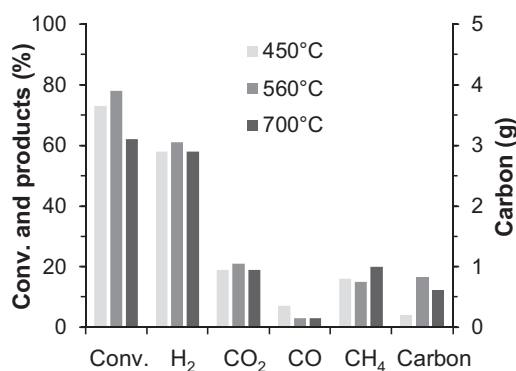


Fig. 10. SRE at 450 °C on the Ni₃Mg₂AlO_y catalyst as a function of treatment temperature in H₂.

observed in the absence or trace amount of metallic cobalt at the surface of the Co–Mg–Al catalyst [34]. As a matter of fact, carbon formation was related to metallic Co while the *in situ* experiment allowed concluding that Co²⁺ species are active for the SRE reaction. The carbon formation follows the increase of ethanol conversion and certainly the increase of metallic Ni.

It has been shown by TPR that higher Ni content decreases the temperature of reduction of Ni species in Ni_xMg₂AlO_y mixed oxides (Fig. 5). Thus the catalyst with higher Ni content may require lower treatment temperature to optimize the activity, selectivity and carbon formation. Therefore the influence of treatment temperature is also investigated on Ni₃Mg₂AlO_y catalyst, representative of a nano-composite with a high Ni content. From Fig. 10, it can be seen that ethanol conversion of about 73% is obtained when the catalyst is treated in H₂ at 450 °C; while if the treatment temperature increases to 700 °C conversion clearly decreases to about 62%. For a treatment temperature in H₂ of 560 °C the conversion slightly increases up to 78%. H₂ and CO₂ formation present almost the same values whatever the treatment temperature. The differences are in CH₄, CO and mainly in carbon formation. Treatment in H₂ at temperatures higher than 450 °C leads to lower CO formation but much higher carbon formation, with the highest carbon formation (0.83 g) observed for a treatment temperature of 560 °C.

The activation of Ni-based catalyst in H₂ is widely accepted as an important factor to influence ethanol conversion, as well as products distribution. In the literature, the pre-treatments of Ni–Mg–Al catalysts were almost performed at very high temperatures (≥ 700 °C) so as to obtain the metallic nickel species that were believed to be the active sites [28,29,36,37]. High temperatures are indispensable to have Ni²⁺ species reduced out of the mixed oxides. But it is of importance to recall that the treatment temperature in our studies can be optimized for each compound in agreement with the shift of TPR peaks. In one case, on the Ni₁Mg₂AlO_y catalyst, the activity significantly increases when treatment temperature

increases from 450 to 700 °C (Fig. 9). However, in another case, on the Ni₃Mg₂AlO_y catalyst, treatment at 700 °C leads to lower ethanol conversion compared to treatment at 450 °C (Fig. 10). But carbon formation is found globally growing with the treatment temperature, and in particular a drastic increase of carbon formation is observed when the treatment temperature is higher than 450 °C. Therefore, in order to easily compare the results, and also balance the conversion and carbon formation, we choose 450 °C as the treatment temperature for Ni_xMg₂AlO_y catalysts in the following study.

3.2.3. The influence of Ni content

Fig. 11 demonstrates the influence of Ni content on the catalytic performances of Ni_xMg₂AlO_y catalysts which are *in situ* treated in H₂ at 450 °C. Ethanol conversion, as well as products distribution, is strongly associated with the Ni content. At a reaction temperature of 450 °C the Mg₂AlO_y compound without the presence of nickel provides 8% ethanol conversion with 43% H₂, 40% acetaldehyde and 17% C₂H₄ formation. The products distribution discloses that the main reactions over the Mg₂AlO_y catalyst are ethanol dehydrogenation and dehydration. As solid inorganic base, Mg–Al hydroxalates are widely applied to the condensation and idolization because of the dehydrogenation and dehydration properties [30]. When small quantity of nickel is added, the Ni_{0.5}Mg₂AlO_y catalyst demonstrates clearly a different catalytic result. Ethanol conversion goes up to 24%, H₂ formation also grows to 64%; while acetaldehyde decreases to 26%, specifically C₂H₄ formation nearly eliminates. Meanwhile, CO₂ (4%), CO (2%) and CH₄ (1%) are observed, suggesting SRE and decomposition start occurring with the presence of nickel. It can be recalled that for this low Ni content, as shown before on the Ni₁Mg₂AlO_y catalyst a higher treatment temperature allows increasing the activity and as reported previously for Co-based compound better results should be obtained [34].

With the increase in Ni content, ethanol conversion and CO₂ formation undergo a global rise, showing that higher Ni content facilitates the SRE process. About 80% conversion and 23% CO₂ are observed at Ni/M_T=0.6. H₂ formation is first analyzed at about 70% when the Ni content is low, and then it decreases to around 55% by increasing the Ni content. Besides, acetaldehyde formation rapidly declines to zero when Ni/M_T equals 0.5, while CH₄ follows similar evolution to CO₂. CO formation exhibits an optimum at Ni/M_T=0.43. The results demonstrate that higher Ni content promotes the decomposition of acetaldehyde and/or ethanol. Carbon formation is observed when Ni/M_T ≥ 0.24 and accelerates with Ni content (Fig. 11). No carbon has been observed on the Ni_{0.5}Mg₂AlO_y catalyst showing that the Ni content can be optimized to avoid carbon formation as previously observed on Co-based catalyst [34].

3.2.4. The efficiency of Ni_xMg₂AlO_y catalyst toward H₂ production

The efficiency of the Ni₃Mg₂AlO_y catalyst toward H₂ production is carefully explored. Fig. 12 reports the time course for the

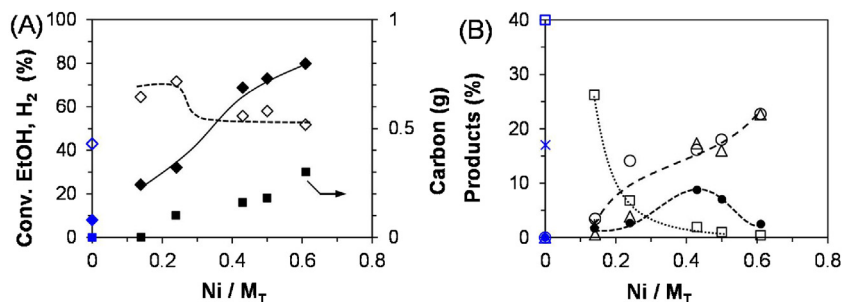


Fig. 11. Influence of Ni content on SRE at 450 °C over Ni_xMg₂AlO_y catalysts pre-treated in H₂ at 450 °C. Ethanol conversion (◆), H₂ (◇), CO₂ (○), CH₃CHO (□), CO (●), CH₄ (△), C₂H₄ (*) and carbon (■) formation. The result presented in blue symbol is for the Mg₂AlO_y compound.

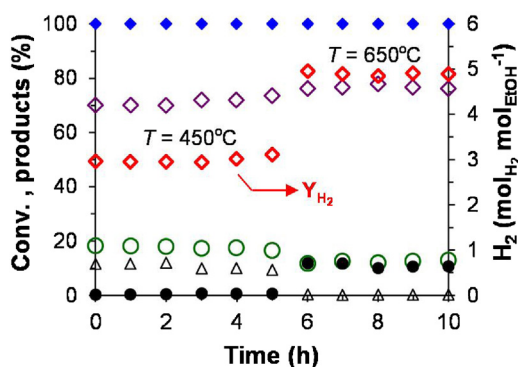


Fig. 12. Efficiency of the $\text{Ni}_3\text{Mg}_2\text{AlO}_y$ catalyst pre-treated in H_2 at 450°C toward H_2 production. Ethanol conversion (\blacklozenge), H_2 (\diamond), CO_2 (\circ), CO (\bullet), CH_4 (\triangle) formation and H_2 yield (\diamond). $\text{EtOH}/\text{H}_2\text{O}/\text{N}_2 = 3/9/88$.

SRE reaction under diluted conditions ($\text{EtOH}/\text{H}_2\text{O}/\text{N}_2 = 3/9/88$) in order to avoid any problem due to the volume variation when a big amount of gases are produced. At 450°C , the $\text{Ni}_3\text{Mg}_2\text{AlO}_y$ catalyst is able to completely convert ethanol and produce the expected products of SRE, i.e. H_2 and CO_2 with the addition of CH_4 . No CO formation is analyzed. A yield to H_2 of $3.0 \text{ mol mol}_{\text{EtOH}}^{-1}$ is obtained in these conditions. This is the highest yield that can be obtained from ethanol alone. None of acetaldehyde or ethylene that could be intermediate is obtained with the time on stream. This shows that the undesirable products of acetaldehyde, ethylene and acetone can vanish over the present catalyst even at relatively low temperature of 450°C . Conversion and selectivity are largely ameliorated compared to the previous results obtained with higher concentration of ethanol. The conversion increase when decreasing the partial pressure of ethanol reflects the partial order to ethanol for this reaction. When reaction temperature further increases up to 650°C , CH_4 formation decreases from about 10% down to almost zero; in the meantime CO formation starts to rise to about 11%. At 650°C the distribution of products obtained (dry basis) corresponds finally to 76% of H_2 , 13% of CO_2 , 11% of CO and 0.2% of CH_4 . Methane reforming is favored at high temperature, whereas water gas shift is favored at low temperature, therefore logically methane decreases with temperature while CO increases [8]. However the very low concentration of methane at only 650°C can be noticed. As a result, the H_2 yield significantly increases up to about $5.0 \text{ mol mol}_{\text{EtOH}}^{-1}$ at 650°C . In such conditions, as expected, hydrogen is formed from ethanol and water. The $\text{Ni}_3\text{Mg}_2\text{AlO}_y$ catalyst shows good stability during at least 10 h of reaction with no signs of deactivation even if carbon species are observed after test. In such conditions (diluted) the quantity of carbon is measured with a formation of 19 mg after 10 h, so a lower value is obtained in diluted conditions.

The H_2 yield of $5.0 \text{ mol mol}_{\text{EtOH}}^{-1}$ obtained on the $\text{Ni}_3\text{Mg}_2\text{AlO}_y$ catalyst at 650°C is one of the best results that have been ever reported for low-cost catalysts. It is important to remark that working at high temperature water gas shift equilibrium does not allow reaching the theoretical value of $6.0 \text{ mol mol}_{\text{EtOH}}^{-1}$. The result obtained here is slightly better, in terms of H_2 yield, than those previously reported, e.g. $4.5 \text{ mol mol}_{\text{EtOH}}^{-1}$ (150 mg of LaNiMgAl catalyst) [26], $4.9 \text{ mol mol}_{\text{EtOH}}^{-1}$ (200 mg of NiMg_4ZnAl catalyst, 700°C) [36]. That is mostly due to the complete methane reforming and relatively lower CO selectivity in our case, which leads to higher H_2 yield. In addition, the ternary $\text{Ni}_x\text{Mg}_2\text{AlO}_y$ catalyst without the extra promoter makes the catalytic system more eco-efficient. Till date some H_2 yields between 4.0 and $5.8 \text{ mol mol}_{\text{EtOH}}^{-1}$ have been reported for low-cost catalysts, especially for Ni-based catalysts, but the values were obtained under conditions in which very high water partial pressure and water to ethanol ratio were used. Our value at 650°C is also better than those reported for

Ni–Zn–Al and Ni–Mg–Al catalysts, taking into account the reaction conditions. Even though H_2 yields of $5.0 \text{ mol mol}_{\text{EtOH}}^{-1}$ ($\text{Ni}_{50}\text{ZnAl}$ catalyst, $\text{H}_2\text{O}/\text{EtOH} = 6$) [27] and $5.1 \text{ mol mol}_{\text{EtOH}}^{-1}$ ($\text{Ni}/\text{Mg}_2\text{Al}$ catalyst, $\text{H}_2\text{O}/\text{EtOH} = 8.4$) [43] were reported, the values were obtained with much higher water–ethanol ratio which has been well known as the promotion to H_2 yield. Compared to other inexpensive catalysts recently reported, such as Co- and Cu-based ex-hydrotalcite mixed oxides, the present result is also competitive. Espinal et al. reported K-promoted CoMg_2Al as stable catalyst for SRE. Total ethanol conversion and H_2 selectivity of 62% was obtained at 550°C with $\text{H}_2\text{O}/\text{EtOH} = 4$ [34]. Lorenz et al. reported that $\text{Cu}/\text{ZnO}/\text{Al}_2\text{O}_3$ showed poor H_2 yield of about $1 \text{ mol mol}_{\text{EtOH}}^{-1}$ at 600°C for SRE [16]. The addition of a second metal (Ni or Co) could significantly improve H_2 yield up to about $5.0 \text{ mol mol}_{\text{EtOH}}^{-1}$ with good stability with a high $\text{H}_2\text{O}/\text{EtOH}$ ratio of 5 [16]. Biswas and Kunzru obtained at 600°C over a $\text{Ni}/\text{CeO}_2\text{–ZrO}_2$ catalyst under a reaction mixture with a high $\text{H}_2\text{O}/\text{EtOH}$ ratio of 8 the highest value for H_2 production ($5.8 \text{ mol mol}_{\text{EtOH}}^{-1}$) that has been reported in the literature, close to the theoretical value of $6 \text{ mol mol}_{\text{EtOH}}^{-1}$ [38]. The other products formed were CO ($0.47 \text{ mol mol}_{\text{EtOH}}^{-1}$), CH_4 ($0.33 \text{ mol mol}_{\text{EtOH}}^{-1}$) and CO_2 ($1.15 \text{ mol mol}_{\text{EtOH}}^{-1}$). Therefore 75% of H_2 were obtained with 6% of CO , 4% of CH_4 and 15% of CO_2 . The present $\text{Ni}_3\text{Mg}_2\text{AlO}_y$ catalyst leads at 650°C with a $\text{H}_2\text{O}/\text{EtOH}$ ratio of 3 to similar H_2 formation (76%) with higher amount of CO (11%), and lower formation of CH_4 that should vary in such a way when increasing reaction temperature. As a matter of fact, thermodynamics predicts the equilibrium composition of reactants and products at different temperatures. Moreover, the increase of the $\text{H}_2\text{O}/\text{EtOH}$ ratio, as well as the addition of He as inert gas increase H_2 production at low temperatures [47,48]. Besides, it is noticeable that the experimental results of H_2 production are higher than the ones calculated by the thermodynamic analysis. It has been reported that there is a region of non-equilibrium in which higher H_2 concentration can be obtained. Moreover, it has been also shown that the carbon formation involving different types of carbon species must also be taken into account in the thermodynamic calculation [47].

3.3. Characterizations of spent $\text{Ni}_x\text{Mg}_2\text{AlO}_y$ catalysts and carbon species

3.3.1. XRD for the spent catalysts

Studying the spent catalysts, as well as the carbon species formed allows further understanding the correlations between the catalyst properties and catalytic performances. Fig. 13 displays the XRD patterns of the spent $\text{Ni}_x\text{Mg}_2\text{AlO}_y$ catalysts. After the SRE reaction in concentrated conditions, the spent catalysts present similarity to those obtained on the catalysts before test (after treatment in H_2). All the phases attributed to NiO , Ni–Mg–(Al)–O and/or MgO are still well maintained. Ni^0 phase with (111) and (200)

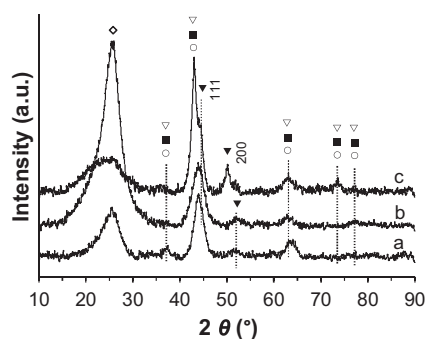


Fig. 13. XRD patterns of the spent $\text{Ni}_x\text{Mg}_2\text{AlO}_y$ catalysts in concentrated conditions at 450°C x= a) 1, b) 3, and c) after SRE in diluted conditions at 650°C . MgO (\circ), Ni–Mg–O (\blacksquare), NiO (∇), Ni (\blacktriangledown), carbon (\diamond).

Table 5
Particles sizes of $\text{Ni}_x\text{Mg}_2\text{AlO}_y$ catalysts.

Catalyst	Conditions	d Oxide crystal/nm ^a	d Ni ⁰ /nm ^b
$\text{Ni}_1\text{Mg}_2\text{AlO}_y$	Calcined at 500 °C	3.6	—
	After SRE at 450 °C	3.7	3.8
$\text{Ni}_3\text{Mg}_2\text{AlO}_y$	Calcined at 500 °C	3.9	—
	Treated in H_2 at 450 °C for 10 h	4.0	4.0
	After SRE at 450 °C	4.2	4.5
	After SRE in diluted conditions at 650 °C	4.4	4.3

^a Calculated from (200) plane.^b Calculated from Ni⁰ (200) plane.**Table 6**
Binding energies and surface Ni molar ratio of the $\text{Ni}_3\text{Mg}_2\text{AlO}_y$ catalyst obtained under different conditions. The full width at half-maximum (FWHM) values of the lines are reported in parentheses.

Catalyst	Conditions	Ni2p _{3/2} /eV	O1s/eV	Ni/M _T
$\text{Ni}_3\text{Mg}_2\text{AlO}_y$	Dried without calcination	856.2 (3.3)	531.7 (2.8)	0.41
	Calcined at 500 °C	855.7 (3.6)	530.6/531.7 (3.1)	0.31
	After SRE at 650 °C	856.5 (5.1)	531.7 (3.7)	0.33

planes is visible in the spent catalysts when $x \geq 1$. Compared with the patterns obtained in H_2 treatment, the intensity is lower. As shown in Fig. 13 when $x = 1$ the quantity of Ni⁰ is low and it increases with Ni content. In diluted conditions the oxide phase and the metallic Ni⁰ phase are clearly seen after test, and the diffraction peaks are better separated. As shown in Table 5 a small particle size is well maintained after test. Solid carbon generated during reactions is in agreement with the presence of a strong diffraction peak due to the graphitic carbon that is visible at $2\theta = 26^\circ$. The intensity of carbon lines appear more intense on the catalysts with higher Ni content, which is in agreement with the carbon formation depending on the Ni content. Moreover, it is in agreement with the results reported before showing that less carbon is observed after test in diluted conditions.

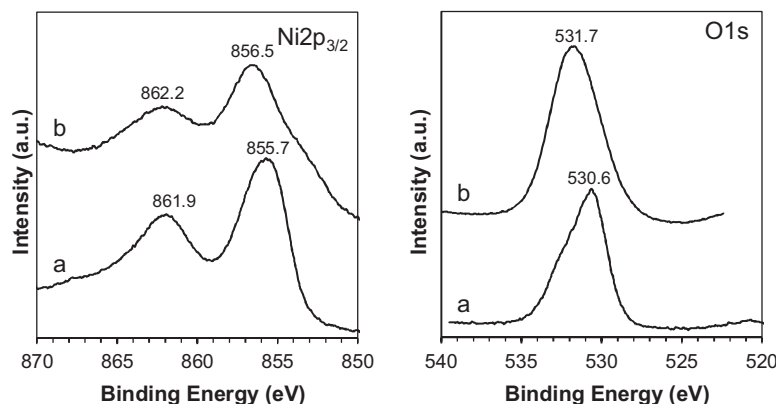
3.3.2. XPS for the spent catalysts

The $\text{Ni}_3\text{Mg}_2\text{AlO}_y$ catalyst is analyzed by XPS after SRE (Fig. 14 and Table 6). A main emission peak in Ni2p_{3/2} region is observed for all the spent catalysts analyzed. Compared to the calcined compounds the binding energies shift to higher values after reaction. The values of the BE obtained after reaction (856.5 eV) become very close to the one obtained on the dried compounds (856.2 eV), in agreement with the value obtained for Ni²⁺ species in Ni(OH)₂ (856.2 eV). This can be well explained by the presence of hydroxyl groups at the surface of the catalyst after reaction in the presence of ethanol and water. Moreover, the characteristic satellite lines of Ni²⁺ species are clearly visible at about 6 eV up to the main peak. After SRE the Ni2p main peak shows higher value for the

full width at half-maximum, which indicates the presence of other Ni species. In fact, a small shoulder peak emerging at lower BE can be assigned to metallic Ni⁰ species on the surface, in agreement with the BE of bulk Ni⁰ species [42]. The surface Ni molar ratios are found lower but still very close to the values obtained on the dried compounds and fresh (calcined) catalysts showing that the homogeneous distribution of Ni species in the catalysts after SRE is relatively well maintained. The O1s spectra are also reported in Fig. 14, while two peaks (530.6 and 531.7 eV) are obtained on the calcined compounds, only one is present after SRE. The value of the BE obtained after reaction (531.7 eV) shifts to higher value (+1.1 eV) compared to the calcined compounds and becomes the same as the one obtained on the dried compounds, even if the full width at half-maximum (FWHM) is higher. This contribution is assigned to oxygen species in OH[−] groups. Therefore, all the oxidized phases are well maintained accompanied with a small amount of metallic Ni phase when increasing Ni content.

3.3.3. O₂-TPO on the carbon species

In order to investigate the characteristic of the carbon species formed on $\text{Ni}_x\text{Mg}_2\text{AlO}_y$ catalysts, O₂-TPO is carried out to provide information about the carbon structure, i.e. amorphous and/or graphitic nature. In the literature, the types of carbonaceous species can be identified by the numbers and position of TPO peaks related to different reactivity toward oxidation. Primarily there is no peak presented at temperatures lower than 400 °C (Fig. 15), which is assigned to the amorphous carbon that is highly reactive toward O₂ and easily oxidized from the nickel surface [49]. It is widely

**Fig. 14.** Ni2p and O1s XPS spectra of the $\text{Ni}_3\text{Mg}_2\text{AlO}_y$ catalyst. a) before reaction, b) after SRE in diluted conditions at 650 °C.

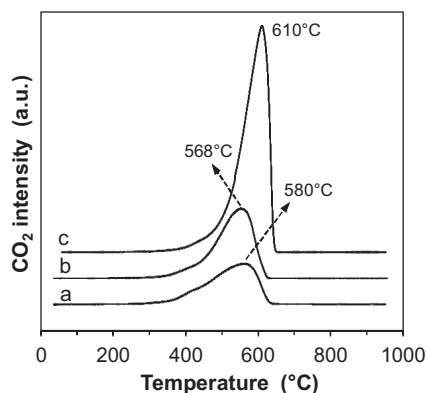


Fig. 15. TPO profiles of the carbon species formed on $\text{Ni}_x\text{Mg}_2\text{AlO}_y$ catalysts during the SRE reaction in concentrated conditions at 450 °C $x = a)$ 1, $b)$ 3, and $c)$ after SRE in diluted conditions at 650 °C.

reported that the single broad peak at around 600 °C is ascribed to more graphitic carbon that is more stable and oxidizes at higher temperatures [49]. In the literature, temperatures around 510 °C were assigned to the single walled carbon nanotubes (SWCNTs), while temperatures around 610 °C could be attributed to the multiwalled carbon nanotubes (MWCNTs). Carbon nanofibers (CNFs) were supposed to burn off in lower temperature range than MWCNTs [49]. As shown in Fig. 15, a single and asymmetric oxidation peak is obtained for all the carbon species formed, which can be generally due to a mixtures of CNFs possibly with some CNTs. Carbon species formed under diluted reactant mixture ($\text{EtOH}/\text{H}_2\text{O}/\text{N}_2 = 3/9/88$) leads to a narrower and more symmetric single peak of about 610 °C, indicating that there might be relatively higher proportion of CNTs in the carbon materials formed.

3.3.4. Raman spectra for the carbon species

Raman spectroscopy has been shown to be an available and powerful technique for characterizing the carbonaceous materials. As reported in Fig. 16, two main peaks well known as the D-band and G-band are visible on all the carbon species analyzed. The D-band observed between 1332 and 1346 cm^{-1} is ascribed to the vibration of the sp^3 hybridized carbon atom with the dangling bonds in the disordered carbonaceous species; while the G-band observed between 1596 and 1600 is assigned to the stretching mode of the sp^2 hybridized carbon atom in the ordered graphite. The way to distinguish between CNFs and CNTs was reported by comparison of the frequency shift, but only slight differences could be verified. The D-band obtained at 1350 cm^{-1} was for CNFs and 1355 cm^{-1} for CNTs; while the G-band was observed at 1592 cm^{-1} on CNFs and 1582 cm^{-1} on CNTs [50]. It has to be remarked that the carbon species analyzed in the present study are without the

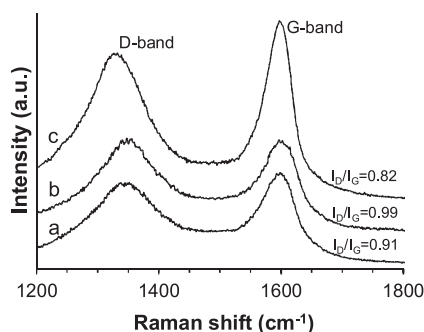


Fig. 16. Raman spectra of the carbon species formed on $\text{Ni}_x\text{Mg}_2\text{AlO}_y$ catalysts during the SRE reaction in concentrated conditions at 450 °C $x = a)$ 1, $b)$ 3, and $c)$ after SRE in diluted conditions at 650 °C.

acid treatment, which might influence the qualitative analysis of carbon structure.

The intensity ratio of D-band to G-band can be quantified as a measure of the degree of graphitization. Hence I_D/I_G is characteristic of the degree of ordered carbon materials. Lower I_D/I_G ratio suggests higher order degree of substances. It is of interest to find out that I_D/I_G ratios depend on the Ni content and reaction conditions, presenting a decrease order of 0.99 ($\text{Ni}_3\text{Mg}_2\text{AlO}_y$) > 0.91 ($\text{Ni}_1\text{Mg}_2\text{AlO}_y$) (concentrated conditions at 450 °C) > 0.82 ($\text{Ni}_3\text{Mg}_2\text{AlO}_y$ in diluted conditions at 650 °C). Lower I_D/I_G ratio is obtained on the catalyst with lower Ni content or on the catalyst tested under highly diluted reactant mixture. In addition, reaction temperature also affects the graphitization of carbon materials formed. The Raman results reach good agreement with the TPO analysis. It proves the formation of the graphitic filamentous carbon species on $\text{Ni}_x\text{Mg}_2\text{AlO}_y$ catalysts during the SRE reaction. As it has been reported previously this type of carbon filaments related to CNFs and/or CNTs can allow a catalytic stability [21,22].

3.4. Active site modeling

In order to understand the correlations between the activity and the overall Ni species in the different catalysts, Fig. 17 reports SRE activity (in mol of ethanol converted per gram of catalyst per hour) measured at 450 °C (14% of EtOH) as a function of the Ni proportion in the compounds. The $\text{Ni}_x\text{Mg}_2\text{AlO}_y$ catalysts activities are found to obey linear evolution increase with Ni content. The highest activity is obtained when Ni content is of 0.6 ($\text{Ni}_4\text{Mg}_2\text{AlO}_y$). Fig. 17 displays also the activity reported in mol. ethanol converted per mol. of nickel per hour, which is obtained by distributing the activity to the Ni molar content in the solids. Reporting activity in this way, it is possible to extract the activity of a mole of Ni species, so the activity of a Ni species in the different solids can be seen. $\text{Ni}_x\text{Mg}_2\text{AlO}_y$ catalysts present a constant activity, which does not vary when the Ni content changes. One Ni species in $\text{Ni}_x\text{Mg}_2\text{AlO}_y$ compounds is able to convert the same amount of ethanol per hour, whatever the $\text{Ni}_x\text{Mg}_2\text{AlO}_y$ compound is. This also suggests that the number of active sites respect very well to the Ni loading. In fact, this is in very good agreement with the XRD and XPS results obtained on $\text{Ni}_x\text{Mg}_2\text{AlO}_y$ compounds. No matter what the Ni content, the compound is ascribed to a mixture of nanoparticles of NiO, MgO and/or to a solid solution of Ni–Mg–(Al)–O. The crystallites sizes of NiO and/or Ni–Mg–(Al)–O maintain in a narrow range of between 3 and 4 nm when Ni loading increases. And there is a homogeneous distribution of Ni in the $\text{Ni}_x\text{Mg}_2\text{AlO}_y$ compounds. Hence more active sites (with the same activity) can be generated in the compound with higher Ni loading. When the Ni content increases, the added Ni species present all the same activity, or in the added Ni species there is always the same proportion of active and inactive Ni species.

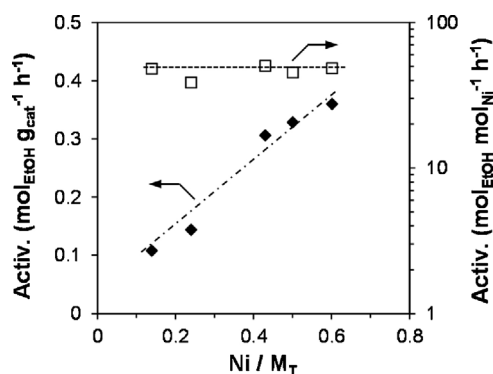
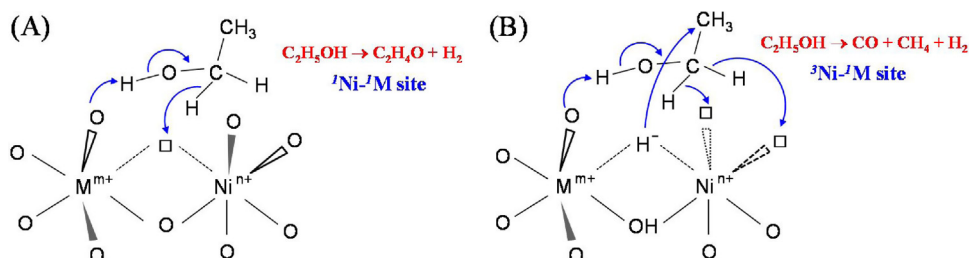


Fig. 17. Activity at 450 °C for SRE (14% of EtOH) of the $\text{Ni}_x\text{Mg}_2\text{AlO}_y$ catalysts pre-treated in H_2 at 450 °C versus Ni content.



Scheme 1. Active site and mechanism modeling of Ni_xMg₂AlO_y catalysts for H₂ production from transformation of bio-ethanol. Niⁿ⁺: Ni²⁺ or Ni^{δ+}; M^{m+}: Mg²⁺ or Al³⁺. (A) ¹Ni-¹M site, (B) ³Ni-¹M site.

The structure of HT-like compounds consists of brucite-like layered double hydroxides where the substitution of M²⁺ with M³⁺ cations leads to a net positive charge, compensated by exchangeable anions in the interlayer space [30]. In brucite (Mg(OH)₂), bivalent cation (e.g. Mg²⁺) and trivalent cations (e.g. Al³⁺) are six-fold coordinated to form octahedral that share edges to constitute infinite layer. Anionic clays in a layer-type lattice as a consequence of the presence of relatively small, two-fold positively charged cations in proximity with polarisable OH⁻ ions. Recently, Ni-based ex-hydrotalcite mixed oxides have been largely reported as good catalysts for SRE [27,36,37,43,51]. The good catalytic activity, selectivity and stability are demonstrated by mainly the strong interactions between Ni species and other cations, e.g. Mg, Al, Zn, Cu and Co. No matter in ternary Ni-Mg-Al, Ni-Zn-Al, Co-Mg-Al and Co-Zn-Al systems [27,43,51], or in Cu-, Zn-promoted Ni-Mg-Al quaternary systems [36,37]; active metals (Ni species and/or Ni-Cu or Ni-Zn bimetals) interact closely with other cations by the incorporation of Ni species into the matrix of other cations, which leads to the small particle sizes, good metal dispersion and high stabilization of the active metal phases with enhanced synergetic effect with other cations.

In the present study, Ni_xMg₂AlO_y ex-hydrotalcite catalysts have shown very strong interactions between Ni species and Mg and/or Al cations either in Ni-Mg-(Al)-O solid solution and/or at the interfaces between small nanoparticles of NiO, MgO and/or Ni-Mg-(Al)-O, evidenced by XRD, XPS, TPR. The H₂ treatment at 450 °C leads to partially reduced solids with simultaneous generation of anionic vacancies. After test the oxide phase is largely recovered. Hence it is reasonable to propose an active site involving an anionic vacancy, an O²⁻ species, and cations in close interaction. Recently, it has been proposed in the literature that Co²⁺ cations are the active site [34] and it is known that anionic vacancies can be created in Mg-Al mixed oxide leading to the presence of coordinatively unsaturated cations [52,53]. If Ni is added into the binary Mg-Al system, of course the number of anionic vacancies that can be created increases. The active site for Ni_xMg₂AlO_y catalysts is modeled in Scheme 1 by an ensemble of two cations (nickel-magnesium or aluminum) in strong interaction, which can be also generally expressed by ^xNi-^yM (where x and y are the unsaturation degrees of each cation), as it has been proposed previously on Ni based catalysts [20] based on a proposed active site for CeNi_xO_y catalysts, the possible mechanism for ethanol transformation can be envisaged on Ni_xMg₂AlO_y compounds. Taking into account the ^xNi-^yM ensemble, for example, at a lower number of anionic vacancies on the site (¹Ni-¹M), acetaldehyde and H₂ can be produced by heterolytic abstraction of hydrogen from ethanol [Scheme 1 (A)]. Each elementary ^xNi-^yM ensemble is associated with a particular reaction. Depending on the unsaturation degree of the active site, conversion of ethanol can lead to different products. As shown in Scheme 1 (B), the ³Ni-¹M site leads to the formation of H₂, CO and CH₄. This model also presents the advantage to be in good agreement with the synergetic effect observed when several cations with strong interactions are in presence in a mixed oxide. Metallic Ni⁰

can also participate in the reaction when it is present; and clearly for the formation of carbon that can be produced from CO [54] and/or CH₄ [55,56], however all the results obtained cannot be explained by simply attributing the activity to this species.

4. Conclusions

Ni_xMg₂AlO_y ex-hydrotalcite mixed oxides synthesized by the co-precipitation method are shown to be highly active heterogeneous catalyst for H₂ production in steam reforming of ethanol. The Ni_xMg₂AlO_y catalysts obtained from the thermal treatment of the hydrotalcite-like precursors turn out to be a type of material with large surface area and uniform metal dispersion. The Ni_xMg₂AlO_y catalysts correspond to mixed oxides with an average particles size varying between 3 and 4 nm. Tuning the Ni content leads to a significant effect on the catalyst properties and catalytic performances. In particular, the reducibility of the catalysts shifts to lower temperatures when increasing the Ni content. The higher Ni content allows obtaining Ni_xMg₂AlO_y catalysts with a higher proportion of active nickel species in small NiO and/or in Ni-Mg-(Al)-O nanoparticles (4 nm). Such nickel species are evidenced to strongly interact with Mg²⁺ and/or Al³⁺ cations, which makes the solid highly reactive for the cleavage of the C-C and C-H bonds. The Ni₃Mg₂AlO_y catalyst *in situ* treated in H₂ at 450 °C demonstrates total ethanol conversion at 450 °C and allows a 3.0 mol mol_{EtOH}⁻¹ H₂ production without formation of CO. A high H₂ yield of 5.0 mol mol_{EtOH}⁻¹ is reported on this catalyst at 650 °C. The H₂ treatment at 450 °C leads to partially reduced solids with simultaneous generation of anionic vacancies. After test the oxide phase is largely maintained. Hence it is reasonable to propose an active site involving anionic vacancies, O²⁻ species, and cations in close interaction. Carbon formation increases with the Ni content and globally with the treatment temperature in H₂. The carbon species formed correspond to graphitic filaments but no deactivation is observed during at least 10 h. Finally, it appears that, the catalyst formulation, activation and the reaction conditions can be optimized according to the desired goal.

Acknowledgments

W. Fang gratefully acknowledges a grant from Erasmus Mundus Tandem. The authors would like to thank Ms. L. Burylo (XRD), Ms M. Trentesaux (XPS), Mr. O. Gardoll (TPR and TPO), and Mr. J. C. Morin (Raman) from UCCS for their valuable technical helps. The "Fonds Européen de Développement Régional (FEDER)", "CNRS", "Région Nord Pas-de Calais" and "Ministère de l'Éducation Nationale de l'Enseignement Supérieur et de la Recherche" are also acknowledged for the funding of XRD analysis.

References

- [1] A. Midilli, M. Ay, I. Dincer, M.A. Rosen, *Renew. Sustain. Energy Rev.* 9 (2005) 273–287.
- [2] M. Momirlan, T.N. Veziroglu, *Int. J. Hydrogen Energy* 30 (2005) 795–802.

- [3] R.R. Davda, J.W. Shabaker, G.W. Huber, R.D. Cortright, J.A. Dumesic, *Appl. Catal. B* 56 (2005) 171–186.
- [4] X. Hu, G. Lu, *Appl. Catal. B* 88 (2009) 376–385.
- [5] D. Li, L. Wang, M. Koike, Y. Nakagawa, K. Tomishige, *Appl. Catal. B* 102 (2011) 528–538.
- [6] P. Azadi, S. Khan, F. Strobel, F. Azadi, R. Farnood, *Appl. Catal. B* 117–118 (2012) 330–338.
- [7] M. Ni, D.Y.C. Leung, M.K.H. Leung, *Int. J. Hydrogen Energy* 32 (2007) 3238–3247.
- [8] L.V. Mattos, G. Jacobs, B.H. Davis, F.B. Noronha, *Chem. Rev.* 112 (2012) 4094–4123.
- [9] N. Bion, D. Duprez, F. Epron, *ChemSusChem* 5 (2012) 76–84.
- [10] S. Maruyama, R. Kojima, Y. Miyauchi, S. Chiashi, M. Kohno, *Chem. Phys. Lett.* 360 (2002) 229–234.
- [11] G. Wang, H. Wang, Z. Tang, W. Li, J. Bai, *Appl. Catal. B* 88 (2009) 142–151.
- [12] D.Z. Mezalira, L.D. Probst, S. Pronier, Y. Batonneau, C. Batiot-Dupeyrat, *J. Mol. Catal. A* 340 (2011) 15–23.
- [13] L. Dai, D.W. Chang, J.-B. Baek, W. Lu, *Small* 8 (2012) 1130–1166.
- [14] K. Park, K.Y. Kim, L. Lu, T.H. Lim, S.A. Hong, H.I. Lee, *Fuel Cells* 7 (2007) 211–217.
- [15] S.M. de Lima, A.M. da Silva, G. Jacobs, B.H. Davis, L.V. Mattos, F.B. Noronha, *Appl. Catal. B* 96 (2010) 387–398.
- [16] B. Lorenz, T. Montini, L. De Rogatis, P. Canton, A. Benedetti, P. Fornasiero, *Appl. Catal. B* 101 (2011) 397–408.
- [17] R. Espinal, E. Taboada, E. Molins, R.J. Chimentao, F. Medina, J. Llorca, *Appl. Catal. B* 127 (2012) 59–67.
- [18] L. Jalowiecki-Duhamel, C. Pirez, M. Capron, F. Dumeignil, E. Payen, *Catal. Today* 157 (2010) 456–461.
- [19] L. Jalowiecki-Duhamel, C. Pirez, M. Capron, F. Dumeignil, E. Payen, *Int. J. Hydrogen Energy* 35 (2010) 12741–12750.
- [20] C. Pirez, M. Capron, H. Jobic, F. Dumeignil, L. Jalowiecki-Duhamel, *Angew. Chem. Int. Ed.* 50 (2011) 10193–10197.
- [21] W. Fang, C. Pirez, M. Capron, S. Paul, T. Raja, P.L. Dhepe, F. Dumeignil, L. Jalowiecki-Duhamel, *RSC Adv.* 2 (2012) 9626–9634.
- [22] W. Fang, C. Pirez, S. Paul, M. Capron, H. Jobic, F. Dumeignil, L. Jalowiecki-Duhamel, *ChemCatChem* 5 (2013) 2207–2216.
- [23] A.J. Vizcaino, P. Arena, G. Baronetti, A. Carrero, J.A. Calles, M.A. Laborde, N. Amadeo, *Int. J. Hydrogen Energy* 33 (2008) 3489–3492.
- [24] L.-C. Chen, S.D. Lin, *Appl. Catal. B* 106 (2011) 639–649.
- [25] M.A. Ebiad, D.R. Abd El-Hafiz, R.A. Elsalamony, L.S. Mohamed, *RSC Adv.* 2 (2012) 8145–8156.
- [26] A.F. Lucrédio, J.D.A. Bellido, E.M. Assaf, *Appl. Catal. A* 388 (2010) 77–85.
- [27] C. Resini, T. Montanari, L. Barattini, G. Ramis, G. Busca, S. Presto, P. Riani, R. Marazza, M. Sisani, F. Marmottini, U. Costantino, *Appl. Catal. A* 355 (2009) 83–93.
- [28] M. Li, X. Wang, S. Li, S. Wang, X. Ma, *Int. J. Hydrogen Energy* 35 (2010) 6699–6708.
- [29] A.J. Vizcaino, M. Lindo, A. Carrero, J.A. Calles, *Int. J. Hydrogen Energy* 37 (2012) 1985–1992.
- [30] F. Cavani, F. Trifirò, A. Vaccari, *Catal. Today* 11 (1991) 173–301.
- [31] A.L. McKenzie, I.C.T. Fishel, R.J. Davis, *J. Catal.* 138 (1992) 547–561.
- [32] A. Corma, V. Fornés, F. Rey, *J. Catal.* 148 (1994) 205–212.
- [33] D.P. Debecker, E.M. Gaigneaux, G. Busca, *Chem. Eur. J.* 15 (2009) 3920–3935.
- [34] R. Espinal, E. Taboada, E. Molins, R.J. Chimentao, F. Medina, J. Llorca, *RSC Adv.* 2 (2012) 2946–2956.
- [35] G.P. Szijjártó, A. Tompos, J.L. Margitfavi, *Appl. Catal. A* 391 (2011) 417–426.
- [36] G. Zeng, Q. Liu, R. Gu, L. Zhang, Y. Li, *Catal. Today* 178 (2011) 206–213.
- [37] X.-P. Yu, W. Chu, N. Wang, F. Ma, *Catal. Lett.* 141 (2011) 1228–1236.
- [38] P. Biswas, D. Kunzru, *Int. J. Hydrogen Energy* 32 (2007) 969–980.
- [39] M. Ogawa, H. Kaiho, *Langmuir* 18 (2002) 4240–4242.
- [40] A. Ponchel, A. Huysse, C. Lamonier, L. Jalowiecki-Duhamel, *Phys. Chem. Chem. Phys.* 2 (2000) 303–312.
- [41] A.P. Grosvenor, M.C. Biesinger, R.St.C. Smart, N.S. McIntyre, *Surf. Sci.* 600 (2006) 1771–1779.
- [42] M.C. Biesinger, B.P. Payne, L.W.M. Lau, A. Gerson, R.St.C. Smart, *Surf. Interface Anal.* 41 (2009) 324–332.
- [43] L.J.I. Coleman, W. Epling, R.R. Hudgins, E. Croiset, *Appl. Catal. A* 363 (2009) 52–63.
- [44] F. Basile, L. Basini, M. D'Amore, G. Fornasari, A. Guarinoni, D. Matteuzzi, G. Del Piero, F. Trifirò, A. Vaccari, *J. Catal.* 173 (1998) 247–256.
- [45] A. Parmaliana, F. Arena, F. Frusteri, N. Giordano, *J. Chem. Soc. Faraday Trans.* 86 (14) (1990) 2663–2669.
- [46] C.H. Bartholomew, R.B. Pannell, J.L. Butler, D.G. Mustard, *Ind. Eng. Chem. Prod. Res. Dev.* 20 (1981) 296–300.
- [47] F. Díaz Alvarado, F. Gracia, *Chem. Eng. J.* 165 (2010) 649–657.
- [48] C.C.R.S. Rossi, C.G. Alonso, O.A.C. Antunes, R. Guirardello, L. Cardozo-Filho, *Int. J. Hydrogen Energy* 34 (2009) 323–332.
- [49] A.W. Musumeci, G.G. Silva, W.N. Martens, E.R. Wacławik, R.L. Frost, *J. Therm. Anal. Calorim.* 88 (2007) 885–891.
- [50] Y. Liu, C. Pan, J. Wang, *J. Mater. Sci.* 39 (2004) 1091–1094.
- [51] R. Guil-López, R.M. Navarro, M.A. Peña, J.L.G. Fierro, *Int. J. Hydrogen Energy* 36 (2011) 1512–1523.
- [52] J.A. Wang, A. Morales, X. Bokhimi, O. Novaro, T. López, R. Gómez, *Chem. Mater.* 11 (1999) 308–313.
- [53] P.V. Sushko, A.L. Shluger, C.R.A. Catlow, *Surf. Sci.* 450 (2000) 153–170.
- [54] X. Yan, C.-J. Liu, *Diam. Relat. Mater.* 31 (2013) 50–57.
- [55] L. Piao, Y. Li, J. Chena, L. Changa, J.Y.S. Lin, *Catal. Today* 74 (2002) 145–155.
- [56] J. Ziebro, I. Łukasiewicz, E. Borowiak-Palen, B. Michalkiewicz, *Nanotechnology* 21 (2010) 145308–145314.